Reconfigurable refraction manipulation at synthetic temporal interfaces with scalar and vector gauge potentials

Han Ye[a,b,1] (iD), Chengzhi Qin[a,b,1], Shulin Wang[a,b,1], Lange Zhao[a,b], Weiwei Liu[a,b], Bing Wang[a,b,2], Stefano Longhi[c,d,2], and Peixiang Lu[a,b,e,2]

Photonic gauge potentials, including scalar and vector ones, play fundamental roles in emulating photonic topological effects and for enabling intriguing light transport dynamics. While previous studies mainly focus on manipulating light propagation in uniformly distributed gauge potentials, here we create a series of gauge-potential interfaces with different orientations in a nonuniform discrete-time quantum walk and demonstrate various reconfigurable temporal-refraction effects. We show that for a lattice-site interface with the potential step along the lattice direction, the scalar potentials can yield total internal reflection (TIR) or Klein tunneling, while vector potentials manifest direction-invariant refractions. We also reveal the existence of penetration depth for the temporal TIR by demonstrating frustrated TIR with a double lattice-site interface structure. By contrast, for an interface emerging in the time-evolution direction, the scalar potentials have no effect on the packet propagation, while the vector potentials can enable birefringence, through which we further create a "temporal superlens" to achieve time-reversal operations. Finally, we experimentally demonstrate electric and magnetic Aharonov–Bohm effects using combined lattice-site and evolution-step interfaces of either scalar or vector potential. Our work initiates the creation of artificial heterointerfaces in synthetic time dimension by employing nonuniformly and reconfigurable distributed gauge potentials. This paradigm may find applications in optical pulse reshaping, fiber-optic communications, and quantum simulations.

gauge-potential interface | synthetical lattice | temporal refraction | Klein tunneling | Aharonov–Bohm effect

Gauge Mpotentials including scalar and vector ones can endow charged particles with a phase shift even without external fields, which is at the heart of the celebrated Aharonov–Bohm (AB) effect (1). Neutral particles such as photons cannot be directly influenced by the gauge potentials. Nevertheless, artificial gauge potentials introduced by creating photonic analogs of AB phases could manipulate the propagation of photons in a similar manner of charged particles. For instance, bended or index-varying waveguide arrays provide a spatially distributed scalar potential, which can yield an effective electric field for enabling various controls over wave diffraction (2–10). On the contrary, electro-optic modulations imposed into resonators or waveguides can give rise to vector potentials by introducing nonreciprocal phase shifts (11–17). These artificial gauge potentials, either for spatially inhomogeneous scalar potentials or time-varying vector potentials, provide powerful tools for emulating the coherent transport dynamics of photons, ranging from Bloch oscillations (2–4), dynamic localization (5–7, 15), to Landau–Zener tunneling (8–10). By judiciously designing the spatial distribution of gauge potentials, artificial magnetic field will also emerge, with which one can create topological edge states and emulate the quantum Hall effect of photons (12, 13). In practical applications, the creation of gauge potentials can also lead to a variety of intriguing light control strategies, such as for realizing negative refraction (14); for one-way light propagation (16); as well as for developing nonreciprocal devices of optical isolators (11), circulators (14), and routers (17).

Recently, vector gauge potentials have been shown to provide a new mechanism of light guiding and localization (18–21), suggesting fresh new ideas in the design of integrated photonic structures with emerging novel functionalities, such as broadband optical switching (22) and dispersionless waveguide coupling (23). Generalized laws of refraction and reflection for discretized light at interfaces between different photonic artificial gauge fields, based on tilted waveguide arrays, have been investigated (24), whereas demonstration of negative refraction by vector gauge potentials has been reported for sound waves (25). However, the simultaneous exploitation and the ability to distinguish scalar and vector potentials for strategic manipulation of light refraction have remained elusive in previous studies, where the main limitations arose from the lack of reconfigurability. Furthermore, some more advanced refraction-related effects such as tunneling and

Significance

Describing electromagnetic field using scalar and vector gauge potentials represents one of the fundamental breakthroughs in classical electrodynamics, which is also at the heart of the celebrated Aharonov–Bohm (AB) effect. Realizing the refraction at gauge-potential interfaces can be harnessed to emulate quantum tunneling effects for photons and to mold the flowing of light. Here, we create a series of gauge-potential interfaces in the temporal lattices and reveal distinct mechanisms for refraction at scalar- and vector-potential interfaces with different orientations. The demonstration of reconfigurable refractions at various gauge-potential interfaces fundamentally expands our capability of manipulating light propagation in synthetic dimensions, which may also find potential applications in the scenarios of optical pulse reshaping, fiber communications, and quantum simulations.

[1]H.Y., C.Q., and S.W. contributed equally to this work.

[2]To whom correspondence may be addressed. Email: wangbing@hust.edu.cn, stefano.longhi@polimi.it, or lupeixiang@hust.edu.cn.

interference occurring at more complex gauge potential interfaces remain largely unexplored.

As a recently emerging field, the photonic lattice in synthetic dimension provides a fertile playground to conveniently tailor the distribution of scalar and vector potentials therein and therefore can serve as a versatile platform to investigate the refraction phenomena with a high degree of reconfigurability. These synthetic lattices can be created by exploiting the internal degrees of freedom of photons, such as frequency (26–33), time (34–39), and orbital angular momentum (40–42). Compared to spatial lattices with fixed potential distributions (43), artificial gauge potentials are more convenient to be introduced into synthetic dimensions and, most importantly, they can be reconfigured on demand. For example, artificial vector potentials can be readily introduced into frequency lattices by controlling the phase of dynamic modulation, leading to the advanced control of spectrum evolution, ranging from frequency diffraction, Bloch oscillations (27), refraction (28), time-reversal operations (30), and even for emulating non-Hermitian topological braiding effects (33). These effects can also be implemented in synthetic temporal lattices constructed by two coupled fiber loops. Thanks to the feasibility in controlling the lattice's features such as the on-site energy, coupling phase, and strength, the temporal lattices possess remarkable advantages in generating scalar and vector potentials, which benefits the demonstration of a variety of classical and quantum effects ranging from parity–time symmetry (34), non-Hermitian skin effect (37), to the topological phase transition (38).

In this work, by creating a synthetic interface of scalar or vector potential in the synthetic temporal lattice, we propose and experimentally demonstrate a series of discrete refraction phenomena in a single and fully reconfigurable setup. It is found that the refraction can be diversely tuned by the orientation of potential interface. As

typical examples, we obtain the temporal total internal reflection (TIR) or Klein tunneling at a scalar-potential lattice-site interface and refraction-free propagation at the vector-potential lattice-site interface. This temporal TIR manifests a nonnegligible penetration depth, which is verified by the frustrated TIR experiment. For an evolution-step interface, we find that scalar potential has no effect on the refraction, while vector potential can enable the temporal birefringence effect. Based on this, we further design a "temporal superlens" and achieve perfect time-reversal operations both for single-site and wave-packet inputs. Finally, we construct a temporal Mach–Zehnder interferometer by utilizing combined lattice–evolution scalar- or vector-potential interfaces and demonstrate the prototypes of electric and magnetic AB effects. The demonstration of reconfigurable refraction at the gauge-potential interfaces fundamentally expands the capability of manipulating wave-packet propagation in synthetic dimensions, with potential applications in optical pulse shaping, fiber communications, and quantum simulations.

Results

Constructions of Scalar and Vector Potentials in the Temporal Lattices. We start from the theoretical model of introducing artificial gauge potentials into synthetic temporal lattices. Consider a coupled fiber-loop circuit, as shown in Fig. 1*A*, where an incident pulse traveling in the longer and shorter loops can be mapped conceptually into a "node-link" model of synthetic temporal lattice, as displayed in Fig. 1*B*. Details of the experimental setup and related theoretical model are given in *SI Appendix*, Sections 1 and 2. The circulating number of the pulses in the fiber loops corresponds to the time-evolution step m in the lattice, and the relative positions of the pulses within one step are denoted by the lattice site n. A pulse hops from step m and position n to step m +
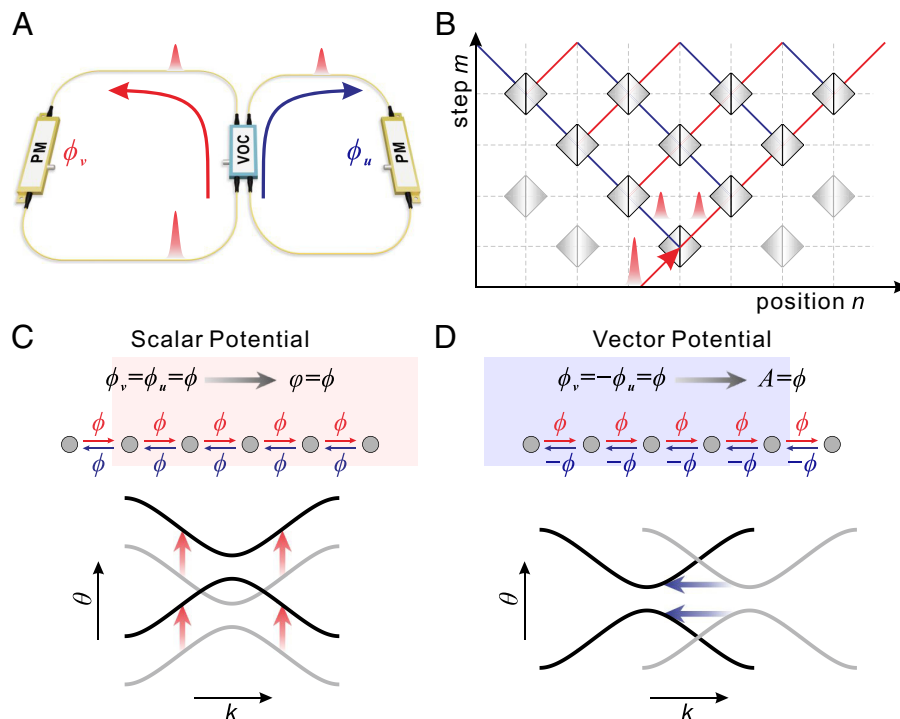

Fig. 1. Experimental implementation of effective scalar and vector potentials in synthetic temporal lattice. (*A*) Schematic sketch of the experimental setup used for implementing synthetic temporal lattice. Two fiber loops with slightly different lengths are connected by a variable optical coupler (VOC). Phase modulators (PMs) in long and short loops control the phase of pulses via ϕ_v and ϕ_u, respectively. The arrows represent the propagation direction of pulses. (*B*) Synthetic temporal lattice mapping from the pulse evolutions in *A*. Red (blue) line indicates rightward (leftward) hopping in the lattice corresponding to a circulation in the long (short) loop. (*C*) Identical phase modulations $\phi_v = \phi_u$ in two loops bring about effective scalar potential φ in synthetical temporal lattice, by which the band structure is shifted vertically. (*D*) Effective vector potential A is mediated by opposite phase modulations $\phi_v = -\phi_u$ in the loops. The band structure undergoes a horizontal displacement in the presence of effective vector potential.

1 and $n - 1$ ($n + 1$) in the lattice after finishing a circulation in the short (long) loop. To introduce a synthetic vector potential, we apply opposite phase modulations $\phi_v = \phi$ and $\phi_u = -\phi$ in long and short loops (21). The pulses then acquire phase shifts of ϕ and $-\phi$ during rightward and leftward hopping. Such a direction-dependent phase shift accompanying light hopping is analogous to a Peierls' phase and corresponds to a vector potential of $A = (\phi_v - \phi_u)/2 = \phi$. On the contrary, when the modulations applied in the two loops are in phase, i.e., $\phi_v = \phi_u = \phi$, the pulse will then acquire identical phase shift during leftward and rightward hopping. Consequently, a synthetic scalar potential $\varphi = (\phi_v + \phi_u)/2 = \phi$ can also be constructed in the lattice. It is worth noting that the construction of vector potentials here is reminiscent of previous studies on creating vector potentials in synthetic frequency dimension (26–32), both requiring direction-dependent phase shifts. However, the construction of scalar potentials using direction-independent phase shift cannot find counterpart in frequency dimension, which is unique to our synthetic temporal lattice. Accordingly, the refractions relying on scalar-potential interfaces cannot be achieved using synthetic frequency lattices.

The pulse evolution in the lattice under scalar and vector potentials is governed by the following evolution equation (Section 2 in *SI Appendix*)

$$u_n^{m+1} = [\cos(\beta)u_{n+1}^m + i\sin(\beta)v_{n+1}^m]e^{i\phi_u},$$
$$v_n^{m+1} = [\cos(\beta)v_{n-1}^m + i\sin(\beta)u_{n-1}^m]e^{i\phi_v}, \quad [1]$$

where u_n^m and v_n^m denote the pulse amplitudes in the short and long loops at step m and position n, respectively, and β is the coupling angle of the coupler. For uniform potentials ϕ_v and ϕ_u, the lattice displays discretized translational symmetries both along the evolution time axis (m axis) and the lattice-extending direction (n axis), so that the eigenstates are of the Floquet–Bloch form: $(u_n^m, v_n^m)^T = (U, V)^T e^{ikn} e^{i\theta m}$, where k and θ are the transverse Bloch momentum and longitudinal propagation constant, respectively. Note that (k, θ) constitutes the two axes in the reciprocal momentum space of the temporal lattice denoted by (n, m). Substituting the eigenmode into Eq. **1**, we can obtain the lattice band structure (*SI Appendix*, Section 2)

$$\theta_\pm(k) = \pm \arccos[\cos(\beta)\cos(k - A)] + \varphi, \quad [2]$$

where $\theta_+(k)$ and $\theta_-(k)$ denote the upper and lower branches of the band, respectively. According to Eq. **2**, one can find that the physical effect of the scalar potential is to induce a propagation constant shift for an eigen Bloch mode, while the vector potential is to induce a Bloch momentum shift. As a consequence, the scalar and vector potentials could induce the total band structure shifts along vertical (quasi-energy) and horizontal (Bloch momentum) directions, as displayed in Fig. 1 *C* and *D*. In the following, we will construct heterointerfaces in the temporal lattice by applying nonuniformly distributed scalar and vector potentials. In terms of interface orientation, we consider two basic types of interfaces: the lattice and evolution ones, which are constructed by introducing an abrupt change of scalar or vector potential along the lattice-extending direction "n" and the time evolution direction "m", respectively. Note that although the lattice-site index n resembles a spatial coordinate, it is physically a time slot index denoting the relative delay or advance between the pulses within one step (see Section 2 in *SI Appendix*). In this sense, both the lattice-site and evolution-step interfaces still belong to temporal interfaces in terms of the physical time

variable. As we will demonstrate below, these two different interfaces can yield a series of distinct refraction effects as light propagates through them.

Refraction at Lattice-Site Interfaces. The lattice-site interface can be constructed by introducing a scalar or vector potential step along the lattice direction "n". We first consider the interface formed by the scalar potentials, which is φ_1 for $n \geq 0$ and φ_2 for $n < 0$, as Fig. 2*A* displays. The potential difference is given by $\Delta\varphi = \varphi_2 - \varphi_1$, for which the band structure undergoes a vertical shift of $\Delta\varphi$ between the two sides of the interface. For a Gaussian-shaped wave-packet incident from the right side ($n > 0$), it will generally experience a refraction at the interface, generating both a refraction and a reflection of wave packet. In direct analogy to the refraction at a spatial interface obeying Snell's law, i.e., the conservation of tangential wave vector along the interface direction, the refraction here along the lattice temporal interface is also governed by the Snell's law, i.e., the conservation of longitudinal propagation constant θ. Specially, for a relatively small (or large) potential difference $\Delta\varphi$, the upper band of the incident packet at right side will match the upper (or lower) band at left side, giving rise to the intraband (interband) tunneling at the interface and hence the occurrence of refraction. Particularly, such an interband tunneling phenomenon provides the temporal analog of Klein tunneling, where a particle tunnels through a potential step without quantum decay by turning into its antiparticle (44). Here in our case, the upper and lower bands just play the roles of the particle and its antiparticle. On the contrary, for a moderate potential difference, the band structure at left side falls into the band gap at the right side, such that the refracted packet vanishes and total internal reflection (TIR) will occur. In experiments, we choose $\Delta\varphi = 0.5\pi$ and 0.8π for demonstrating the above two cases, where the refraction processes are shown in Fig. 2 *A* and *B*. For $\Delta\varphi = 0.5\pi$, no refracted beam exists, clearly indicating the occurrence of TIR. While for $\Delta\varphi = 0.8\pi$, the Klein tunneling occurs. Also note that the refracted beam manifests a direction derivation with respect to the incident one, suggesting the abrupt change of group velocity during the refraction process. Finally, by continuously varying $\Delta\varphi$ from 0 to 2π, we also obtain the general formula of the power transmission coefficient (44) (*SI Appendix*, Section 3)

$$T_\pm = \frac{(1 - e^{2\lambda_0})(1 - e^{\pm 2\lambda_2})}{(\pm 1 - e^{\lambda_0} e^{\pm \lambda_2})^2}, \quad [3]$$

where $\lambda_0 = \text{arsinh}[\cot(\beta)\sin(k_i)]$ and $\lambda_2 = \text{arsinh}[\cot(\beta)\sin(k_t)]$, with k_i and k_t being the Bloch momenta of the incident and refraction packets, respectively. "+(−)" denotes that the refracted packet appears in the upper and lower bands, corresponding to the intraband and interband tunneling cases. The reflection is then given by $R = 1 - T$. The transmission/reflection coefficients are determined by the incident Bloch momentum and the relative scalar potentials at two sides. The results here are also similar to spatial refractions described by Fresnel's equations, where the transmission/reflection coefficients are determined by the incident angle and the relative refraction indices at both sides of the interface. The measured transmission and refraction coefficients are also shown by the red and blue dots in Fig. 2*C*, respectively, which can coincide well with the theoretical curves. Specially, the TIR occurs in the regions of $0.25\pi < \Delta\varphi < 0.75\pi$ and $1.25\pi < \Delta\varphi < 1.75\pi$, outside of which the refraction can take place (*SI Appendix*, Section 4).
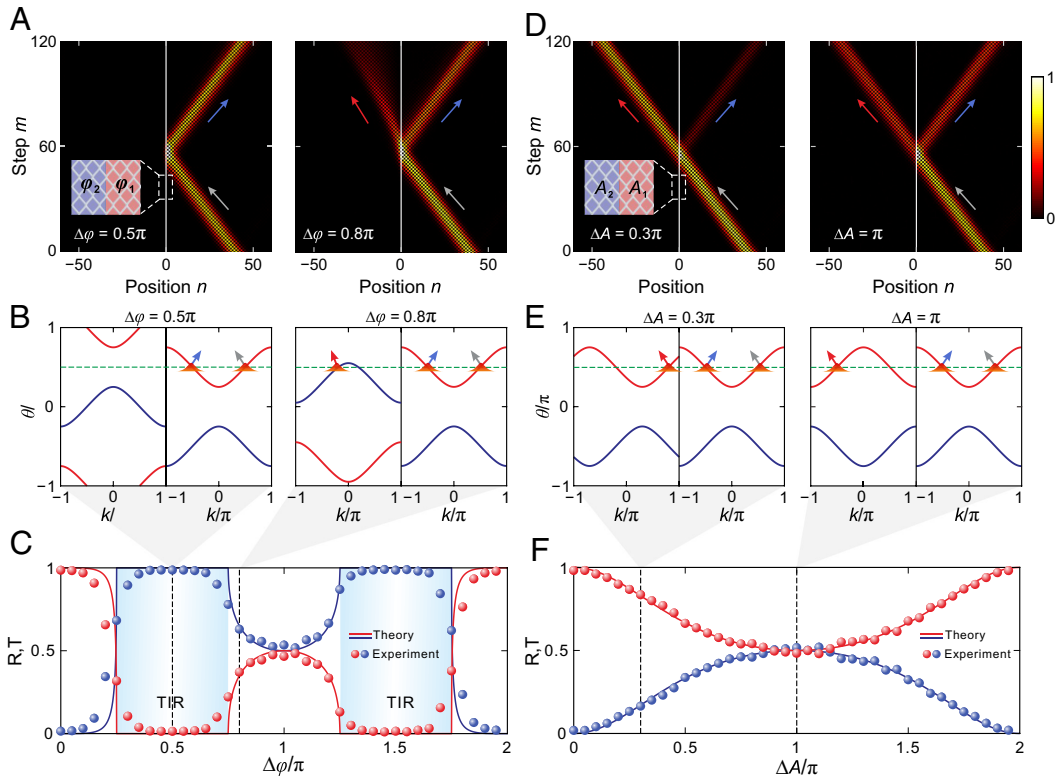
Fig. 2. Refractions at the lattice-site interfaces. (*A*) Measured pulse intensity evolution as a wave packet impinges the lattice-site interface constructed by scalar potentials. The inset shows the distribution of scalar potentials. The potential difference is given by $\Delta\varphi = \varphi_2 - \varphi_1$, which is fixed at 0.5π for the left panel and 0.8π for the right panel. (*B*) Band structures in two sides of the interface at $\Delta\varphi = 0.5\pi$ and 0.8π. Green dashed line represents the propagation constant conservation. The gray, blue, and red arrows indicate propagation directions of the incident, reflected, and transmitted wave packets, respectively. (*C*) Theoretical (solid line) and measured (circle) transmission T (red) and reflection R (blue) coefficients as a function of $\Delta\varphi$. (*D*) Measured pulse intensity evolution at lattice-site interface constructed by vector potentials. The potential difference in the left and right panels is $\Delta A = 0.3\pi$ and π. The inset illustrates the distribution of vector potential. (*E*) The band structures at $\Delta A = 0.3\pi$ and π. (*F*) Theoretical (solid line) and measured (circle) transmission T (red) and reflection R (blue) coefficients versus ΔA.

On the contrary, the lattice-site interface can also be constructed by substituting φ_1 and φ_2 with A_1 and A_2, such that the potential difference becomes $\Delta A = A_2 - A_1$. The band structure at the left side will undergo a horizontal shift of ΔA with respect to that at the right side. Likewise, by applying Snell's law, i.e., the longitudinal propagation constant conservation, one can find that refraction will always exist due to the complete band structure's overlap at two sides, thus preventing the occurrence of TIR. In experiments, we choose $\Delta A = 0.3\pi$ and π, where beam refraction and reflection are always observable, as shown in Fig. 3 *D* and *E*. Moreover, in contrast to the above lattice-site interface formed by scalar potentials where the refracted packet experiences an abrupt group velocity change, the packet here can maintain its propagation direction at the lattice-site interface formed by vector potentials. The general transmission coefficient is given by (*SI Appendix*, Section 5)

$$T = \frac{\cosh(2\lambda_0) - 1}{\cosh(2\lambda_0) - \cos(\Delta A)}. \quad [4]$$

The transmission and reflection versus ΔA are shown in Fig. 2*F*. The transmission reaches minimum at $\Delta A = \pi$ and one cannot observe TIR like that in the interface constructed by scalar potentials.

The TIR in temporal lattice here is reminiscent of its counterpart in real space. A prominent feature of spatial TIR is the existence of evanescent wave penetrating the reflection interface at a wavelength-scale depth. Here, we design a frustrated total internal reflection (FTIR) scenario as a criterion to verify the existence of evanescent wave accompanying our temporal TIR. We construct

a double lattice-site interface structure composed of a narrow gap with scalar potential φ_2 and width Δn sandwiched by two semi-infinite regions with scalar potential φ_1, as shown in Fig. 3 *A* and *B*. The potential difference is thus $\Delta\varphi = \varphi_2 - \varphi_1$, which is fixed at $\pi/2$ in our implementation. The incident wave packet is injected from the right side and experiences TIR at the first interface. Similar to the real-space TIR, the packet can partially penetrate to the gap region. If the gap is narrow enough, the wave can further penetrate to the left side of the gap. The tunneling process is analogous to the FTIR in real space. As $\Delta n = 2$, the gap is relatively large and there are seldom waves transmitted. Most of the waves are reflected by the interface. However, if we decrease the gap width to $\Delta n = 1$, the beam can partially penetrate to the left region. The transmission coefficient versus the gap width is shown in Fig. 3*C*, which decreases gradually with the increase of gap width. The experiment clearly verifies that the penetration depth is at a scale of $\Delta n \sim 1$ for our temporal TIR.

Refraction at Evolution-Step Interfaces. As another interface orientation, an evolution-step interface can also be constructed by introducing a potential step along the direction of time evolution. We first consider the interface formed by scalar potentials, which are assumed to be φ_1 for $m \leq 60$ and φ_2 for $m > 60$, as Fig. 4*A* displays. The potential difference is given by $\Delta\varphi = \varphi_2 - \varphi_1$. As the wave packet is incident from the bottom, its propagation is not influenced by the interface, as shown in Fig. 4*A*. Figure 4*B* depicts the band structure of the top region, which undergoes a vertical shift of $\Delta\varphi = \pi$ with respect to the bottom region. For the evolution-step interface, the Snell's law is that the transverse Bloch
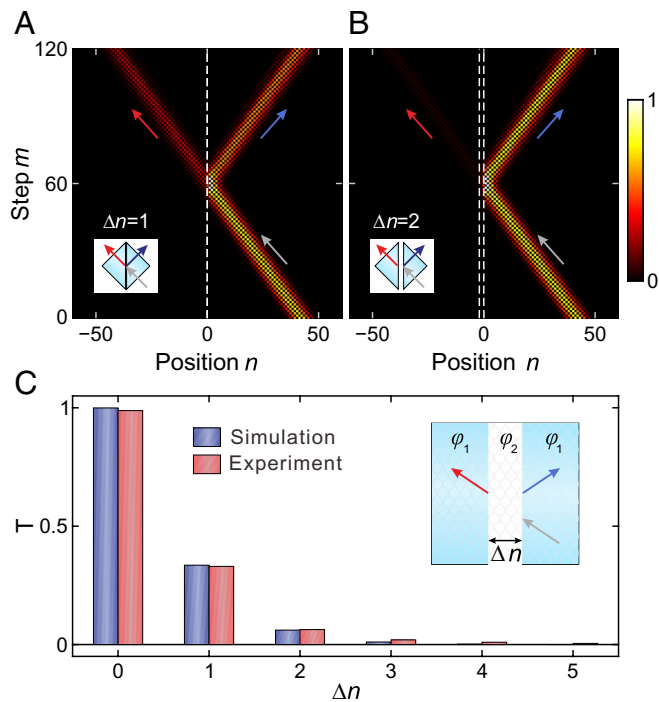
Fig. 3. Temporal FTIR. (*A* and *B*) The measured pulse intensity evolutions as Δn = 1 (*A*) and 2 (*B*). The insets show the schematic diagrams of the FTIR. (*C*) Measured (red bars) and simulated (blue bar) transmission coefficients as a function of the gap width Δn. The inset shows the distribution of scalar potentials.

momentum should be conserved. Still considering the incidence of an upper band mode, it will excite the mode at the same band in the top region. The influence of Δφ on the band occupancies in the top region is depicted in Fig. 4*C*. One sees that the occupancies are independent on Δφ and remain the same with that in the bottom region. The output field intensities are measured at *m* = 120 and the profile keeps unchanged as Δφ varies, experimentally

verifying the triviality of evolution-step interface constituted by scalar potentials, as illustrated in Fig. 4*D*.

The evolution-step interface can also be constructed by introducing vector potentials. As shown in Fig. 4*E*, the vector potentials are assumed to be A_1 for $m \leq 30$ and A_2 for $m > 30$. The potential difference reads $\Delta A = A_2 - A_1$. For $\Delta A = \pi/2$, the incident wave packet splits into two branches with opposite propagation directions. The band structure in the top region undergoes a horizontal shift by $\Delta A = \pi/2$, as depicted in Fig. 4*F*. Likewise, the Bloch momentums along the lateral position direction should also be conserved. For the incidence of an upper band mode, the modes of upper and lower bands in the top region are generated simultaneously, with their occupancies P_+ and P_- given by (*SI Appendix*, Section 6)

$$P_{\pm} = \frac{\cosh(\lambda_0 \pm \lambda_1) \pm \cos(\Delta A)}{2\cosh(\lambda_0)\cosh(\lambda_1)}, \qquad [5]$$

where $\lambda_0 = \text{arsinh}[\cot(\beta)\sin(k_i)]$ and $\lambda_1 = \text{arsinh}[\cot(\beta)\sin(k_i - \Delta A)]$. As ΔA varies from 0 to 2π, the measured data of P_+ and P_- are depicted in Fig. 4*G*, which can coincide well with the theoretical analysis. For $\Delta A = \pm\pi/2$, the upper and lower band occupancies are identical, where the incident wave packet splits equally into two branches. The output field intensity measured at $m = 120$ undergoes an oscillating transverse motion as ΔA varies, as illustrated in Fig. 4*H*. This can be well explained by the opposite periodic variations of the group velocities of the upper and lower band modes, $v_{g,\pm} = \partial\theta_{\pm}(k-\Delta A)/\partial k$ as ΔA varies. The beam splitting here is analogous to the time refraction and reflection at a temporal interface, which is induced by an abrupt change of refraction index at specific time instant in a spatially homogeneous medium (45, 46). Here, the split wave packet occupying the lower band corresponds to the reflected beam, while the other one occupying the upper band corresponds to the refracted beam. Unlike the models of Refs. (45, 46), where the time dimension is continuous, our temporal lattice is discrete both in the lattice (*n*) and evolution (*m*) directions. Accordingly, the time refraction and reflection in
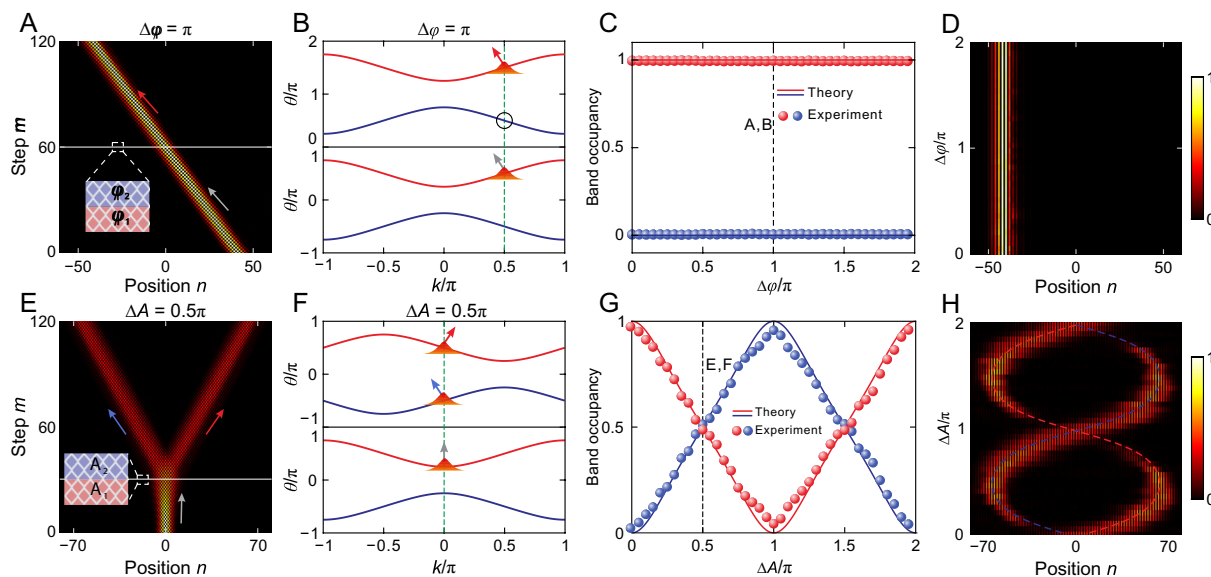

Fig. 4. Refractions at evolution-step interfaces. (*A*) Measured pulse intensity evolution as Δφ = π. The inset shows the distribution of scalar potentials at the evolution-step interface. (*B*) The band structures of the two sides at Δφ = π. The Bloch momentum conservation is indicated by green dashed line. (*C*) Measured (circle) and theoretical (solid line) upper band (red) and lower band (blue) occupancies versus Δφ in the top region. (*D*) Measured output field intensity at *m* = 120 as a function of Δφ. (*E*) Measured pulse intensity evolution for ΔA = 0.5π. (*F*) The band structures in the top and bottom regions at ΔA = 0.5π. (*G*) Measured (circle) and theoretical (solid line) upper band (red) and lower band (blue) occupancies versus ΔA as the wave packet crosses the interface. (*H*) Measured output field intensity distribution at *m* = 120 as a function of ΔA.
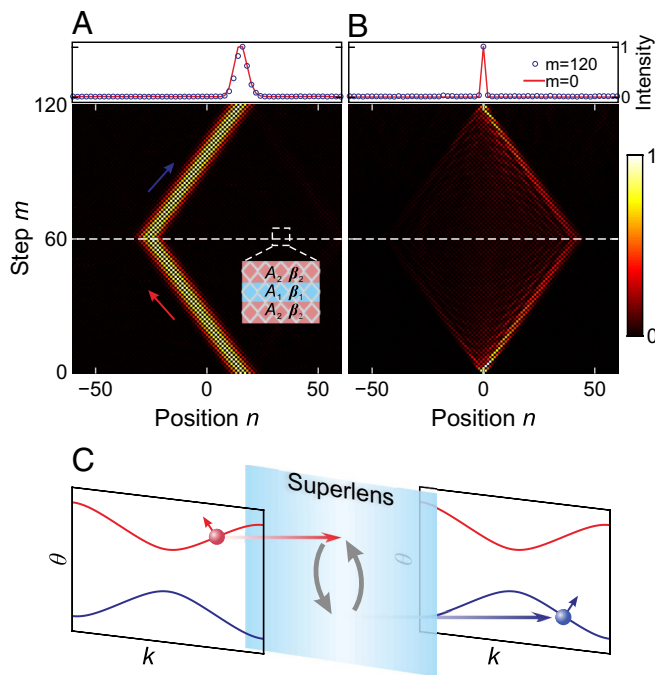
Fig. 5. Time reversal induced by band occupancy inversion. (*A*) Measured pulse intensity evolution for a wave packet incidence. The inset figure shows the distribution of vector potentials and coupling parameters. Measured intensity profiles at time step $m = 0$ and $m = 120$ are displayed on the upper panel. (*B*) Measured pulse intensity evolution for a single-site excitation. (*C*) The abrupt change of vector potential and coupling parameter at time step $m = 60$ can be viewed as a superlens for exchange of eigenstates.

our system act to a discretized pulse train, rather than to continuous light waves as in refs. 45 and 46. The evolution-step interface of gauge potentials in temporal lattice opens a new avenue to emulate refraction and reflection in a synthetic time dimension with full reconfigurability, which is hard to implement in continuous spatial systems.

By taking advantage of the evolution-step interface formed by vector potential steps, we can realize time reversal of pulse evolution. As shown in Fig. 5*A*, a vector potential of A_1 is applied in the time interval Δm beginning from $m = 60$ during the pulse evolution and that in the rest is denoted by A_2. The potential difference between adjacent regions is thus $\Delta A = A_2 - A_1$. In order to manipulate the band structures more flexibly, the coupling ratio of the fibers is also changed with time, which is set as β_1 in the disturbed time interval Δm and the rest is set as β_2. Here, we choose $\Delta m = 1$, $\Delta A = \pi/2$, $\beta_1 = \pi/2$, and $\beta_2 = \pi/4$. For the incidence of a Gaussian-shaped wave packet with a Bloch momentum $k = \pi/2$ in the upper band, it moves backward initially and undergoes a mirror reversion after passing through the disturbed time interval, featuring negative refraction. Note that only a single time step is utilized to vary the vector potential and coupling ratio while the undisturbed regions on both sides are identical. Therefore, the temporal interface mimicked by a single time step behaves as a superlens with infinitesimal thickness in real space. The temporal superlens is also applicable to the imaging of a point source that contains all Fourier components, i.e., Bloch modes in the whole Brillouin zone. As shown in Fig. 5*B*, for a single pulse incidence, i.e., for excitation of a single lattice site at $n = 0$, discrete diffraction is observed at the first region, with subsequent refocusing onto a single site after passing through the superlens. Note that there exists perceptible asymmetry in the imaging pattern along the lattice direction. This is attributed to the unequal excitation of upper and lower bands from single-loop incidence. Since each Bloch-wave component in upper and lower bands possesses

opposite group velocities, their interference with unequal band occupations gives rise to this asymmetric evolution pattern. To obtain symmetric evolution patterns, we need to simultaneously excite from both fiber loops with appropriate relative amplitude and phase. The imaging effect can be explained by the reversion of Bloch modes. As the wave packet passes through the interface, the Bloch mode in the upper band converts to the lower one as we change both the gauge potential and the coupling ratio within a single time step, as illustrated in Fig. 5*C*. The group velocity undergoes a mirror reversion after passing through the temporal superlens. The details can be found in *SI Appendix* (*SI Appendix, Section 7*).

Electric and Magnetic AB Effects. In the above implementations, we apply a scalar or vector potential alone and have experimentally verified their unique and distinct functionalities in manipulating temporal refractions at a specific interface. In this section, we show that the combination of lattice and evolution scalar- or vector-potential interfaces can benefit to the construction of a Mach–Zehnder interferometer (MZI) in time dimension, and hence for emulating the celebrated electric and magnetic AB effects. As depicted in Fig. 6 *A* and *B*, the electric and magnetic AB effects can be accomplished by using MZI applied with scalar and vector gauge potentials, respectively. The gauge potential difference, and hence the phase difference between the two arms, determines the final output intensity. In our setup, we utilize a lattice-site interface at $n = 0$ formed by vector potentials to play the role of 50:50 beam splitter and a superlens at $m = 60$ for the beam reversal operation, as shown in Fig. 6*C*. The beam interference at the output end is thus determined by the total phase difference in the two arms, consisting of the propagation phases accumulating in the two paths and the abrupt phase jumps acquired at the lattice-site interface at $n = 0$ and evolution-step interface at $m = 60$. First, we consider the MZI without propagation phase. Taking the rightward output beam, along path 1, the packet acquires a phase jump of π for reflection, 0 at the superlens and π for reflection at output end, giving rise to total phase jump of $\phi_1 = \pi + 0 + \pi = 2\pi$. For path 2, the phase jump is 0 for transmission, π at the superlens, and π for transmission at output end, such that $\phi_2 = 0 + \pi + \pi = 2\pi$. So, the phase jump difference between the two paths is $\phi_1 - \phi_2 = 0$, which gives rise to the constructive interference (*SI Appendix, Section 8*). Similar procedure is also applicable to the analysis of the destructive interference for the leftward output beam.

Based on this, we then introduce the propagation phase to simulate AB effects. First, a scalar potential difference is imposed on the interferometer arms. The scalar potentials in the two arms are denoted by φ_1 for $n < 0$ and φ_2 for $n > 0$. The potential difference is denoted by $\Delta\varphi = \varphi_1 - \varphi_2$. In the experimental implementation, the scalar potentials are applied at $30 \leq m < 90$ with a time interval $\Delta m = 60$, as depicted in Fig. 6*D*. Then, the accumulated phase should be $\Delta\phi = \Delta m \Delta\varphi$. As $\Delta\phi = \pi$, the output intensities of wave packets undergo a constructive interference and the output intensity reaches maximum at $n < 0$. By varying $\Delta\varphi$, the wave packet will appear at a symmetric position $n > 0$ and the intensity experiences a periodic oscillation, as illustrated in Fig. 6*E*. The magnetic AB effect can also be implemented by employing MZI applied with vector potentials, as depicted in Fig. 6*F*. A vector potential difference is imposed on the interferometer arms. The vector potentials are assumed to be A_1 in $30 \leq m < 60$ and A_2 in $60 < m \leq 90$, both with a time length $\Delta m = 30$. The potential difference reads $\Delta A = A_1 - A_2$. From Fig. 6*F*, one sees that the accumulated phase difference should be $\Delta\varphi = 2\Delta n \Delta A$, where $\Delta n = v_g \Delta m$ with the group velocity $v_g = \sqrt{2}/2$. As $\Delta\phi = \pi$; the
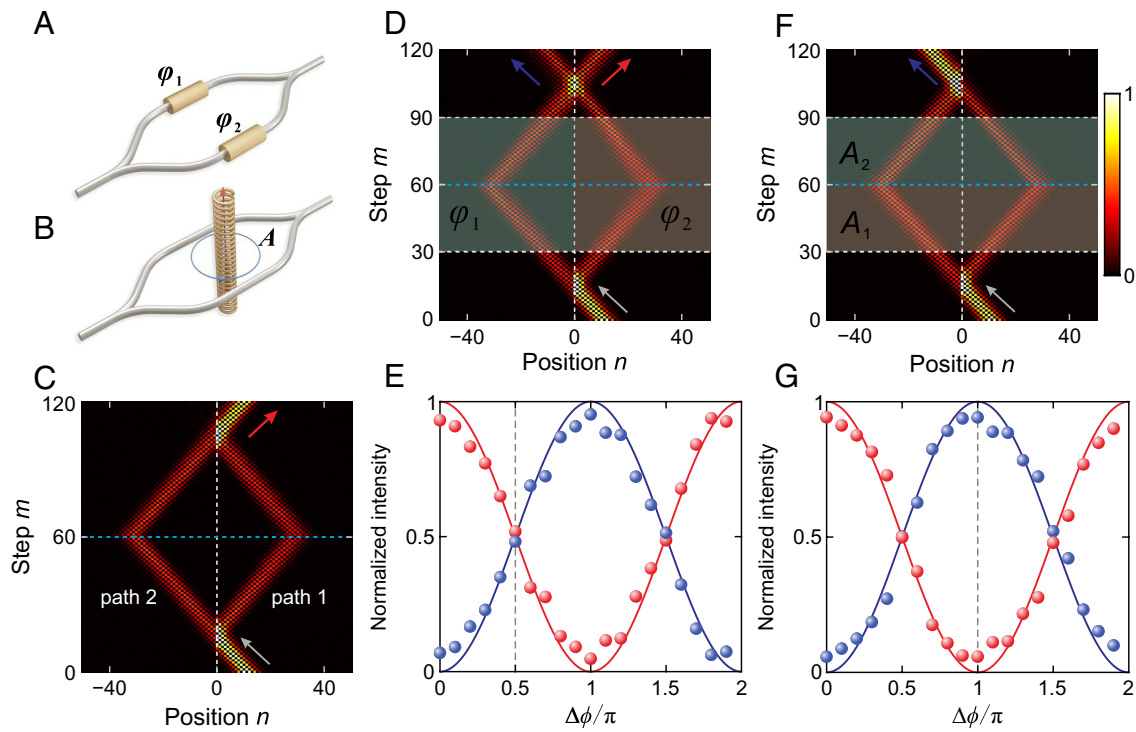
Fig. 6. Electric and magnetic Aharonov–Bohm (AB) effects. (*A* and *B*) Schematic diagram of the electric (*A*) and magnetic (*B*) AB effects. (*C*) Temporal Mach–Zehnder interferometer constructed by combined lattice-site and evolution-step interfaces. The gray and cyan dashed lines represent vector potential interface and superlens, respectively. The gray and red arrows indicate the incident and output wave packets, respectively. (*D*) Measured pulse intensity evolution for electric AB effect as accumulated phase difference between two arms is $\Delta\phi = \pi/2$. (*E*) Measured (circles) and theoretical (solid curves) normalized intensity of outputs on the left (blue) and right (red) sides of the lattice-site interface as a function of $\Delta\phi$. (*F* and *G*), Same as (*D* and *E*) but for magnetic AB effect.

wave packets also undergo a constructive interference at $n < 0$ while a deconstructive interference at $n > 0$, as illustrated in Fig. 6*F*. When $\Delta\phi$ varies from 0 to 2π, the output intensities corresponding to the superposed wave packets with backward and forward evolutions are measured. The data are depicted in Fig. 6*G*, where the output intensities vary as a function of $\Delta\phi$ sinusoidally, evidently verify the interference affected by the vector potentials.

Conclusion

In summary, we have experimentally constructed reconfigurable lattice-site and evolution-step interfaces using inhomogeneous scalar and vector potentials in the temporal lattice, by which the unique features of refraction processes with respect to these two potentials are demonstrated in a reconfigurable setup. The TIR and FTIR mediated by scalar potential at the lattice-site interface are achieved, while the transmission always exists for vector potential. The vector potential redistributes the band occupancies at the evolution-step interface, resulting in wavepacket splitting upon impinging the interface. By abruptly changing the vector potentials in a single time step, we also construct an evolution superlens and demonstrate perfect time-reversal operation of pulse evolution. We further emulate the celebrated electric and magnetic AB effects by virtue of the combined lattice-site and evolution-step interfaces. Our results reveal the uniqueness of scalar and vector potentials in controlling the refraction of wave packets at synthetic interfaces and demonstrate the ability to reconfigure the refraction scenario, realizing different functionalities with the same device. Moreover, due to the flexibility in designing the interface orientation and configuration, our system is expected to serve as an ideal platform to emulate various quantum mechanical

phenomena such as quantum tunneling effects. Finally, the fully reconfigurable temporal refraction could lead to many applications of pulse reshaping, multiplexing, and manipulation used for optical communication and quantum information processing, where reconfigurability and functional complexity have become increasingly demanding.

Materials and Methods

Experimental Implementation. The experimental setup comprises of two fiber loops which are connected by a variable optical coupler (VOC), as Fig. 1*A* displays. The coupling ratio between the two loops can be controlled by applying electric signal on the VOC via an arbitrary waveform generator (AWG). Each loop comprises a spool of single-mode fiber, corresponding to the average round-trip time of approximately 25 μs for the two loops. The length difference between the two loops is introduced by inserting an additional optical fiber patch cord in the long loop, which gives rise to a time difference of approximately 0.15 μs between the round-trip times in the two loops. To feed the circuit, a 50 ns long pulse is coupled into the long loop, which is prepared by modulating the output light beam from a 1,550 nm distributed-feedback laser. During the circulation in the loops, the optical loss can be compensated by erbium-doped fiber amplifiers (EDFAs) in the two loops. To suppress the transient of the EDFA, the signal pulses are mixed with a high-power 1,530 nm pilot light before entering the EDFA. After the EDFA, the pilot light and spontaneous emission noise in the amplification process are removed by a band-pass filter. Besides, we employ the polarization beam splitter and polarization controllers in the loops to monitor and control the polarization of the light signal. The optical isolators are used to ensure the unidirectional circulation in loops. The Mach–Zehnder intensity modulators in fiber loops serve as optical switches. The phases of pulses are controlled by phase modulators in the loops, which are driven by AWGs. Because of the flexible tunability of electric signal generated by AWGs, the effective gauge potentials deriving from the phase modulations in two loops can be arbitrarily constructed in the synthetic temporal lattice. In order to detect and record the pulse evolutions in the two loops, we couple a

small portion of light signals from both loops and detect them with photodetectors. The output voltages of the photodetectors are sampled by an oscilloscope. A more detailed description of the experimental platform is included in *SI Appendix* (*SI Appendix*, Section 1).

Data, Materials, and Software Availability. All study data are included in the article and/or supporting information.

Author affiliations: [a]Wuhan National Laboratory for Optoelectronics and School of Physics, Huazhong University of Science and Technology, Wuhan 430074, China; [b]Optics Valley Laboratory, Hubei 430074, China; [c]Dipartimento di Fisica, Politecnico di Milano, Piazza Leonardo da Vinci 32, I-20133 Milano, Italy; [d]IFISC (UIB-CSIC), Instituto de Fisica Interdisciplinar y Sistemas Complejos, E-07122 Palma de Mallorca, Spain; and [e]Hubei Key Laboratory of Optical Information and Pattern Recognition, Wuhan Institute of Technology, Wuhan 430205, China

1. Y. Aharonov, D. Bohm, Significance of electromagnetic potentials in the quantum theory. *Phys. Rev.* **115**, 485–491 (1959).
2. U. Peschel, T. Pertsch, F. Lederer, Optical Bloch oscillations in waveguide arrays. *Opt. Lett.* **23**, 1701–1703 (1998).
3. G. Lenz, I. Talanina, C. M. de Sterke, Bloch oscillations in an array of curved optical waveguides. *Phys. Rev. Lett.* **83**, 963–966 (1999).
4. T. Pertsch, P. Dannberg, W. Elflein, A. Bräuer, F. Lederer, Optical Bloch oscillations in temperature tuned waveguide arrays. *Phys. Rev. Lett.* **83**, 4752–4755 (1999).
5. S. Longhi *et al.*, Observation of dynamic localization in periodically curved waveguide arrays. *Phys. Rev. Lett.* **96**, 243901 (2006).
6. A. Szameit *et al.*, Polychromatic dynamic localization in curved photonic lattices. *Nat. Phys.* **5**, 271–275 (2009).
7. A. Joushaghani *et al.*, Generalized exact dynamic localization in curved coupled optical waveguide arrays. *Phys. Rev. Lett.* **109**, 103901 (2012).
8. H. Trompeter *et al.*, Visual observation of Zener tunneling. *Phys. Rev. Lett.* **96**, 023901 (2006).
9. S. Longhi, Optical Bloch oscillations and Zener tunneling with nonclassical light. *Phys. Rev. Lett.* **101**, 193902 (2008).
10. F. Dreisow *et al.*, Bloch-Zener oscillations in binary superlattices. *Phys. Rev. Lett.* **102**, 076802 (2009).
11. K. Fang, Z. Yu, S. Fan, Photonic Aharonov-Bohm effect based on dynamic modulation. *Phys. Rev. Lett.* **108**, 153901 (2012).
12. K. Fang, Z. Yu, S. Fan, Realizing effective magnetic field for photons by controlling the phase of dynamic modulation. *Nat. Photonics* **6**, 782–787 (2012).
13. S. Mittal *et al.*, Topologically robust transport of photons in a synthetic gauge field. *Phys. Rev. Lett.* **113**, 087403 (2014).
14. K. Fang, S. Fan, Controlling the flow of light using the inhomogeneous effective gauge field that emerges from dynamic modulation. *Phys. Rev. Lett.* **111**, 203901 (2013).
15. L. Yuan, S. Fan, Three-dimensional dynamic localization of light from a time-dependent effective gauge field for photons. *Phys. Rev. Lett.* **114**, 243901 (2015).
16. K. Fang *et al.*, Generalized non-reciprocity in an optomechanical circuit via synthetic magnetism and reservoir engineering. *Nat. Phys.* **13**, 465–471 (2017).
17. C. Qin, A. Alù, Z. J. Wong, Pseudospin-orbit coupling for chiral light routings in gauge-flux-biased coupled microring resonators. *ACS Photonics* **9**, 586–596 (2022).
18. Q. Lin, S. Fan, Light guiding by effective gauge field for photons. *Phys. Rev. X* **4**, 031031 (2014).
19. S. Slussarenko *et al.*, Guiding light via geometric phases. *Nat. Photonics* **10**, 571–575 (2016).
20. Y. Lumer *et al.*, Light guiding by artificial gauge fields. *Nat. Photonics* **13**, 339–345 (2019).
21. A. V. Pankov, I. D. Vatnik, D. V. Churkin, A. A. Sukhorukov, Observation of localized modes at effective gauge field interface in synthetic mesh lattice. *Sci. Rep.* **9**, 3464 (2019).
22. I. A. D. Williamson, S. Fan, Broadband optical switch based on an achromatic photonic gauge potential in dynamically modulated waveguides. *Phys. Rev. Appl.* **11**, 054035 (2019).
23. W. Song *et al.*, Dispersionless coupling among optical waveguides by artificial gauge field. *Phys. Rev. Lett.* **129**, 053901 (2022).
24. M.-I. Cohen *et al.*, Generalized laws of refraction and reflection at interfaces between different photonic artificial gauge fields. *Light Sci. Appl.* **9**, 200 (2020).
25. Y. Yang *et al.*, Demonstration of negative refraction induced by synthetic gauge fields. *Sci. Adv.* **7**, eabj2062 (2021).
26. L. Yuan, Y. Shi, S. Fan, Photonic gauge potential in a system with a synthetic frequency dimension. *Opt. Lett.* **41**, 741–744 (2016).
27. L. Yuan, S. Fan, Bloch oscillation and unidirectional translation of frequency in a dynamically modulated ring resonator. *Optica* **3**, 1014–1018 (2016).
28. C. Qin *et al.*, Spectrum control through discrete frequency diffraction in the presence of photonic gauge potentials. *Phys. Rev. Lett.* **120**, 133901 (2018).
29. A. Dutt *et al.*, A single photonic cavity with two independent physical synthetic dimensions. *Science* **367**, 59–64 (2020).
30. C. Qin, B. Wang, Z. J. Wong, S. Longhi, P. Lu, Discrete diffraction and Bloch oscillations in non-Hermitian frequency lattices induced by complex photonic gauge fields. *Phys. Rev. B* **101**, 064303 (2020).
31. H. Chen *et al.*, Real-time observation of frequency Bloch oscillations with fibre loop modulation. *Light Sci. Appl.* **10**, 48 (2021).
32. J. Yang *et al.*, Phonon-induced anomalous gauge potential for photonic isolation in frequency space. *Optica* **8**, 1448–1457 (2021).
33. K. Wang, A. Dutt, C. C. Wojcik, S. Fan, Topological complex-energy braiding of non-Hermitian bands. *Nature* **598**, 59–64 (2021).
34. A. Regensburger *et al.*, Parity-time synthetic photonic lattices. *Nature* **488**, 167–171 (2012).
35. M. Wimmer, H. M. Price, I. Carusotto, U. Peschel, Experimental measurement of the Berry curvature from anomalous transport. *Nat. Phys.* **13**, 545–550 (2017).
36. M. Wimmer, U. Peschel, Observation of time reversed light propagation by an exchange of eigenstates. *Sci. Rep.* **8**, 2125 (2018).
37. S. Weidemann *et al.*, Topological funneling of light. *Science* **368**, 311–314 (2020).
38. S. Weidemann, M. Kremer, S. Longhi, A. Szameit, Topological triple phase transition in non-Hermitian Floquet quasicrystals. *Nature* **601**, 354–359 (2022).
39. S. Wang *et al.*, High-order dynamic localization and tunable temporal cloaking in ac-electric-field driven synthetic lattices. *Nat. Commun.* **13**, 7653 (2022).
40. F. Cardano *et al.*, Detection of Zak phases and topological invariants in a chiral quantum walk of twisted photons. *Nat. Commun.* **8**, 15516 (2017).
41. X. W. Luo *et al.*, Synthetic-lattice enabled all-optical devices based on orbital angular momentum of light. *Nat. Commun.* **8**, 16097 (2017).
42. L. Yuan *et al.*, Photonic gauge potential in one cavity with synthetic frequency and orbital angular momentum dimensions. *Phys. Rev. Lett.* **122**, 083903 (2019).
43. A. Szameit *et al.*, Fresnel's laws in discrete optical media. *New J. Phys.* **10**, 103020 (2008).
44. S. Longhi, Klein tunneling in binary photonic superlattices. *Phys. Rev. B* **81**, 075102 (2010).
45. E. Lustig *et al.*, "Towards photonic time-crystals: Observation of a femtosecond timeboundary in the refractive index" in *2021 Conference on Lasers and Electro-Optics (CLEO)* (IEEE, Piscataway, NJ, 2021), pp. 1–2.
46. H. Moussa *et al.*, Observation of temporal reflections and broadband frequency translations at photonic time-interfaces. arXiv [Preprint] (2022). https://arxiv.org/abs/2208.07236 (Accessed 1 August 2022).